A Coarse-Grained Model for the Mechanical Behavior of Na-Montmorillonite Clay

Sarah Ghazanfari ¹ [+], H. M. Nasrullah Faisal ² [+], Kalpana S. Katti ^{1,2,3}*,

Dinesh R. Katti ^{1,2,3}*, Wenjie Xia ^{1,2}*

¹ Department of Civil, Construction, Environmental Engineering, North Dakota State University, Fargo, ND 58108, United States

² Materials and Nanotechnology, North Dakota State University, Fargo, ND 58108, United States

³ Center for Engineered Cancer Testbeds, North Dakota State University, Fargo, ND 58108, United States of America

[+] These authors contributed equally to this work

* To whom correspondence should be addressed.

Contact information:

wenjie.xia@ndsu.edu (W.X.)

dinesh.katti@ndsu.edu (D.K.)

kalpana.katti@ndsu.edu (K.K.)

ABSTRACT

Sodium montmorillonite (Na-MMT) is one of the most commonly found swelling clay minerals with diverse engineering and technological applications. The nanomechanical properties of this mineral have been extensively investigated computationally utilizing molecular dynamics (MD) simulations to portray the molecular-level changes at different environmental conditions. As the environmentally found Na-MMT clays are generally sized within hundreds of nanometers, allatomistic MD simulations of clays within such size range are particularly challenging due to computational inefficiency. Informed from atomistic modeling, coarse-grained (CG) modeling technique can be employed to overcome the spatiotemporal limitation. The current study presents a CG modeling strategy to develop a computationally efficient model of Na-MMT clay with a typical size over ~100 nm by shrinking the atomistic platelet thickness and reducing the number of center-layer atoms. Using the "strain-energy conservation" approach, the force field parameters for the CG model are obtained and the developed CG model can well preserve in-plane tension, shear, and bending behaviors of atomistic counterparts. Remarkably, the CG tactoid model of Na-MMT, a hierarchical multilayer structure, can reproduce the interlayer shear and adhesion, as well as d-spacing among the clay sheets as of atomistic one to a good approximation, while gaining significantly improved computational speed. Our study demonstrates the efficacy of the CG modeling framework, paving the way for bottom-up multiscale prediction of mechanical behaviors of clay and related minerals.

Keywords: Montmorillonite Clay, Molecular Dynamics Simulation, Coarse-Grained Modeling, Mechanical properties.

1. INTRODUCTION

Sodium montmorillonite (Na-MMT) clay, a 2:1 aluminum phyllosilicate has long been attracting researchers due to its unique swelling behavior in the presence of water. This montmorillonite clay can expand up to 15 times its original volume when the swelling is allowed. However, it exerts a large amount of pressure when the swelling is constrained. High swelling pressure causes damage to buildings, foundations, highways, dams, etc.^{1,2} The swelling behavior of Na-MMT clay has been utilized in geoenvironmental engineering, polymer clay nanocomposites, and the mining industry. Geosynthetic clay liner (GCL), a barrier material used in landfills, contains MMT clay as an integral constituent due to its high fluid storage capability.^{3,4} Addition of a small proportion of organically modified MMT clays results in significant improvement of thermal and mechanical responses of polymeric materials.⁵⁻⁹ Therefore, modeling the behavior of montmorillonite clays can provide us with a better understanding of their properties at a molecular level.

Na-MMT clay is composed of a hierarchical structure. Different experimental measures inspecting the clay porosities referred to the multiscale structure of clays. ^{10–14} A tetrahedral SiO₄ (T) and octahedral AlO₆ (O) sheet (TOT) clay layer is the fundamental building block of Na-MMT clay. Isomorphous substitution of aluminum (Al³⁺) ions from the octahedral sheet by iron (Fe²⁺) or magnesium (Mg²⁺) ions develops the charge deficiency in the clay layer. This phenomenon is neutralized by interlayer Na cations. ^{15,16} The basal spacing or d-spacing of Na-MMT clay is generally considered as 10 Å. Tactoid is a clay particle that is built up of 10 clay layers stacked in the thickness direction. ^{17,18} Several clay tactoids are rolled or crumpled to form a clay aggregate of 0.1 microns. At the uppermost stage of clay hierarchical structure, a number of clay aggregates are combined in different directions to form multiple aggregates (>10 microns). ¹⁰ Investigation of clay hydration sites also exhibited the various stages of clay structure. ¹⁹ In addition to the multi-

scale structural features of clays, significant variations of clay particle size have been reported based on experiments. Transmission electron microscopy (TEM) micrograph of Na-MMT clay particle showed that the particle size can range from a few nanometers to several hundred nanometers.^{20–22} Atomic force microscopy (AFM) imaging of Na-MMT clay particles revealed the existence of two distinct sized populations of Na-MMT clay particles, i.e., the average length and width of larger-sized particles are 340 nm and 200 nm, respectively.²¹

In parallel to experimental investigation, molecular dynamics (MD) simulations have been increasingly utilized to explore the molecular features of clay minerals and relevant materials at a fundamental level.^{23–28} For instance, molecular interactions with various fluids, hydration behavior, and nanomechanical properties of montmorillonite clays have been successfully investigated through MD simulations by employing atomistic clay models with nanoscopic dimensions.^{29–35} To perform the atomistic MD modeling of clay, various force fields have been developed and utilized, including ClayFF, InterfaceFF, CementFF, ReaxFF, URF, etc. 36,37 Among these force fields with several pros and cons, ClayFF is so far the most commonly implementable force field for clay minerals, but it treats a significant amount of bonded interactions as non-bonded ones along with some misrepresentation of internal multipole moments due to the inaccuracy of some atomic charge assignment (e.g. Si). 38,39 InterfaceFF is considered the most reliable due to its accurate partial charges while it is limited in simulating chemical reactions.^{39–41} ReaxFF can model the bond breaking/formation, where chemical reaction and fracture behaviors could be simulated, but the computational cost is very heavy.⁴² CementFF is applicable to all cementitious systems while it causes excessive restructuring and water-density fluctuations as a full-atomic charge force field.43

Despite the usefulness of atomistic MD simulations, it is challenging to simulate larger clay layer model to mimic the behavior of real-sized (tens ~ hundreds of nm) clay particles. Moreover, the clay particle needs to be represented by a clay tactoid in which multiple clay layers are typically stacked in the vertical direction, resulting in a model system having millions of atoms. This is essentially challenging for atomistic MD simulations of such massive atomistic models, which would require significant computing resources. These particular scale-related issues need to be addressed for bottom-up modeling of clay systems based on MD simulations. He for this purpose, coarse-grained (CG) modeling is often used to bridge the spatiotemporal limitations of atomistic systems by reducing the number of degrees of freedom and removal of fine interaction details. This simplification is achieved by clustering a number of atoms into one super-bead (i.e., heavy pseudo CG bead), and the effective interactions among the CG beads need to be derived by preserving the essential features and physical behaviors of the reference systems. The effectively developed CG model allows simulation and prediction of physical performance of complex systems with access to extended time and length scales.

Different researchers have taken different routes to perform the CG modeling of clays. A number of prior studies employed both continuous and discrete modeling approaches with a view to performing coarse-grained simulations of clay minerals.^{49–51} The pseudo-atoms procedures utilizing Iterative Boltzmann Inversion (IBI) were used to perform coarse-graining of polymer-clay composite systems through seven different CG bead types.^{52,53} Several studies also performed the ultra-continuous coarse-grained modeling of clay minerals in which a number of clay platelets are modeled as a single particle.^{54,55} A structural CG model made up of five different beads was parameterized using the IBI algorithm to mimic the properties of atomistic anhydrous clay.⁵⁶ An extension of the MARTINI force field named MARTINIFF employing four different beads in

which three heavy atoms defined as one bead was used to build the CG model of organically modified MMT clay whose parameters were derived from mechanical properties and cleavage energy of atomistic clay particles.⁵⁷ Despite progress made, it is still difficult to overcome the spatiotemporal limitation of clay modeling using those previous CG models.

In the current study, we aim to present an effective strategy to develop a computationally efficient CG model of Na-MMT clay using a single common bead type for the whole structure of a clay layer. Informed from the all-atomistic (AA) modeling of clay based on the ClayFF, the bonded parameters of the CG clay model will be derived from the intra-layer (intra-platelet) mechanical properties while the non-bonded parameters will be obtained from inter-layer adhesion energy. Then the mechanical response of the CG clay stack (tactoid) including tensile, in-plane shear, bending, interlayer shear, and compression will be determined utilizing these parameters and cross-validated with the atomistic tactoid model. Finally, to show the performance of the computational efficiency of our CG model, the CPU time is calculated and compared for different clay sheet sizes in both AA and CG model systems.

2. COARSE-GRAINING STRATEGY

2.1. Overview of an atomistically informed CG model

The construction of a CG model is based on the simplification of the all-atomistic (AA) model of MMT clay platelet with a t-o-t layered structure, where an alumina octahedral sheet is sandwiched between two silica tetrahedral sheets. As shown in **Figure 1A**, silicon ions are at the center of the silica tetrahedral sheet while aluminum ions are at the center of the alumina octahedral sheet. These silicon and aluminum ions can be viewed as the backbone of the clay platelet, forming hexagonally arranged lattice structures. Every one of four aluminum ions is isomorphically substituted by iron or magnesium ions. The length of one side of the hexagon is calculated as 3.051

Å. The angle and dihedral angles are computed as 120° and 180° respectively. Hexagonality has been found as the primary structural feature of backbone cations of clay platelet. To construct the CG model, we first build one-layer clay platelet by only considering the lattice positions of aluminum ions (with isomorphic substitutions) of the octahedral sheet. As illustrated in Figure 1A and B, the cyan beads are representative of octahedral cations (Al, Fe, Mg) that carry the mass of all atoms in the clay layer where the total mass of the clay layer is equally distributed among the cyan (initial) beads. This leads to a mass of 183.43 amu for each cyan bead. Then, every four neighbor aluminum cations (as marked by the triangle region in Figure 1B) are grouped into one CG bead with the center of mass placed on the position of the center junction aluminum. The choice of the AA-to-CG mapping allows us to preserve the hexagonal lattice structure in the CG model with enlarged lattice spacing (Figure 1C). The resulting bond length of CG beads that form the larger hexagon is 6.102 Å, which is exactly twice the distance between cations of the octahedral layer. The bending angle among the three CG beads is 120° and the dihedral angle between four beads is 180°. The mass of the CG bead is then determined by preserving the total mass of the atomistic platelet for a given size under coarse-graining. This leads to a mass of 733.72 amu (= 4×183.43) for each CG bead having the same type (i.e., the red beads presented in Figure 1C and **Figure 1D**). Finally, **Figure 1D** shows a representative CG model of $10 \times 10 \text{ nm}$ (20×11) clay sheet consisting of 229 CG beads, corresponding to 8,800 atoms in the AA system.

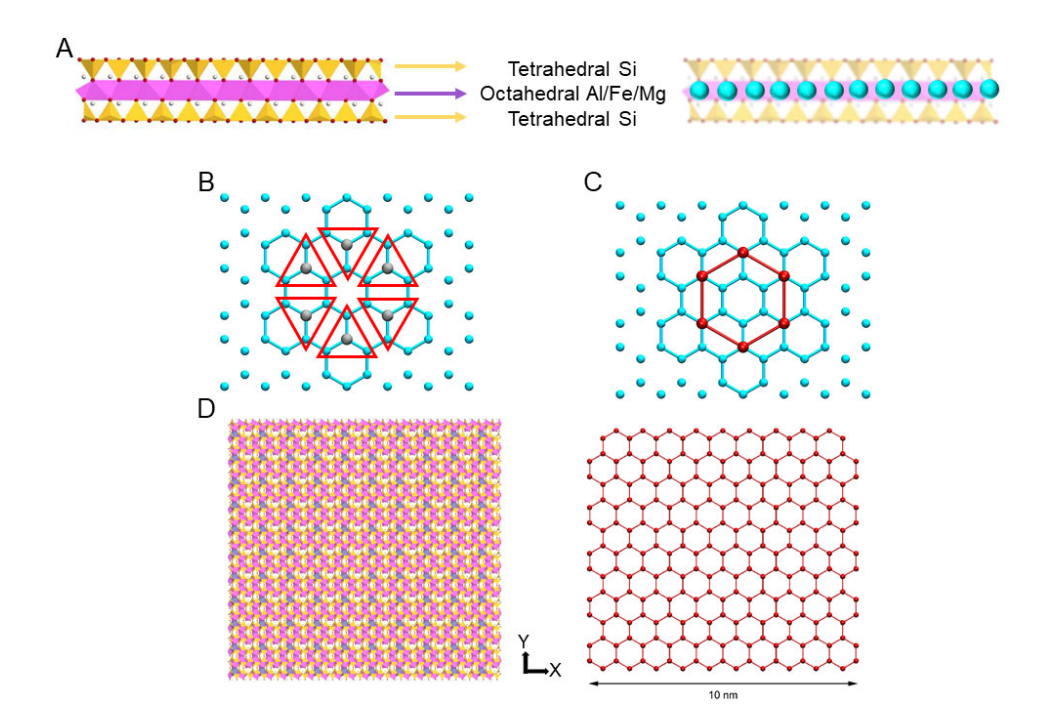


Figure 1. Different stages of CG clay model building from the atomistic model. (A) Two tetragonal layers and one octahedral layer (t-o-t) make up the montmorillonite clay platelet. Only the octahedral center cations (Al/Fe/Mg) (i.e., marked as cyan beads) are considered for the first fold of coarse-graining with an enlarged concentrated mass of 183.43 amu per bead. (B) Four neighbor cyan beads within an imaginary triangle region are further grouped together and the junction/center is identified as the force center of the CG bead (in red) with a mass of 733.72 amu. (C) The junction of masses/beads is connected to form a larger hexagon lattice. (D) Mapping from the atomistic to CG model of 10 nm Na-MMT sheet.

2.2. Development of CG force field

In this work, the CG force field is derived from the underlying AA clay model using the strainenergy conservation approach. This approach has been successfully adopted to develop several other CG models, such as graphene and other nanoparticles.⁵⁸ The resulting CG force field includes both internal (bonded) and external (non-bonded) interactions. The total energy function (E_T) has the following form:

$$E_T = E_b + E_a + E_d + E_{nb} \tag{1}$$

where E_b , E_a , E_d , E_{nb} are the energies of bonds, angles, dihedrals, and non-bonded interactions of the whole system respectively. The functional forms of each term are presented below:

$$E_{\rm b}(r) = k_r(r - r_0)^2 \tag{2}$$

$$E_a(\theta) = k_\theta (\theta - \theta_0)^2 \tag{3}$$

$$E_d(\varphi) = k_{\varphi}[1 + \cos(n\varphi - \delta)] \tag{4}$$

$$E_{nb}(r) = 4\varepsilon \left[\left(\frac{\sigma}{r} \right)^{12} - \left(\frac{\sigma}{r} \right)^{6} \right], \quad r < r_{cut}$$
 (5)

where k_r, k_θ, k_ϕ are the bond, angle, and dihedral angle force constants, respectively; r_0 and θ_0 are equilibrium distance of the bond and equilibrium angle, respectively; δ is the phase dihedral angle and n is an integer constant; ε is the well depth of Lennard-Jones (LJ) 12-6 potential, σ is zero-crossing distance for the LJ potential and r_{cut} is the cutoff distance of the LJ potential. The relation between the distance where the LJ potential reaches its energy minimum (R_{min}) and σ can be estimated as $R_{min} = 2^{\frac{1}{6}} \sigma$.

There are totally eight independent parameters in the CG force field, i.e., k_r , k_θ , k_φ , r_0 , θ_0 , δ , ε and σ , which need to be determined. Three out of these 8 parameters include r_0 , θ_0 and δ are related to the lattice geometry of the CG model and are predetermined based on the adopted AA-to-CG mapping as mentioned above: $r_0 = 6.102 \,\text{Å}$, $\theta_0 = 120^\circ$ and $\delta = 180^\circ$. The other five parameters can be determined by evaluating the in-plane mechanical and interlayer properties of the AA model as described next.

As mentioned above, to calibrate the CG model, the mechanical properties of the atomistic model are needed which is mainly influenced by its strain energy density function.⁵⁹ Therefore, a strain energy conservation approach is utilized. According to this approach, mechanical and physical properties of AA clay are needed to determine the CG force field parameters, including elastic tensile modulus (E), in-plane shear modulus (S), bending rigidity (κ) and adhesion energy per surface area (U_a) . To this end, we utilize Steered Molecular Dynamics (SMD)⁶⁰ to determine elasticity, in-plane shear, and bending properties. SMD provides a platform to induce conformational changes in systems in order to study the variation of the potential of mean force (PMF). The setting for the equilibration process and SMD calculation will be described in the following section. A 10 nm AA clay sheet is taken into consideration to calculate the required mechanical properties. To determine its elasticity, the left side of the clay sheet along the x-axis is kept fixed and the right side is pulled along the x-axis (Figure 2A). The average tensile modulus for this model is found to be 695.8 GPa. Next, to investigate the in-plane shear modulus, the left side of the clay sheet along the x-axis is kept fixed while the right side is pulled along the y-axis, see **Figure 2B.** The average in-plane shear modulus is computed as 137.2 GPa by taking the ratio of in-plane shear stress and strain. The bending rigidity is found to be 2.8×10⁻¹⁷ N·m through a 3point bending test on clay sheet by fixing two edges of clay sheets and imposing line force to the midpoint of clay sheet (Figure 2C).

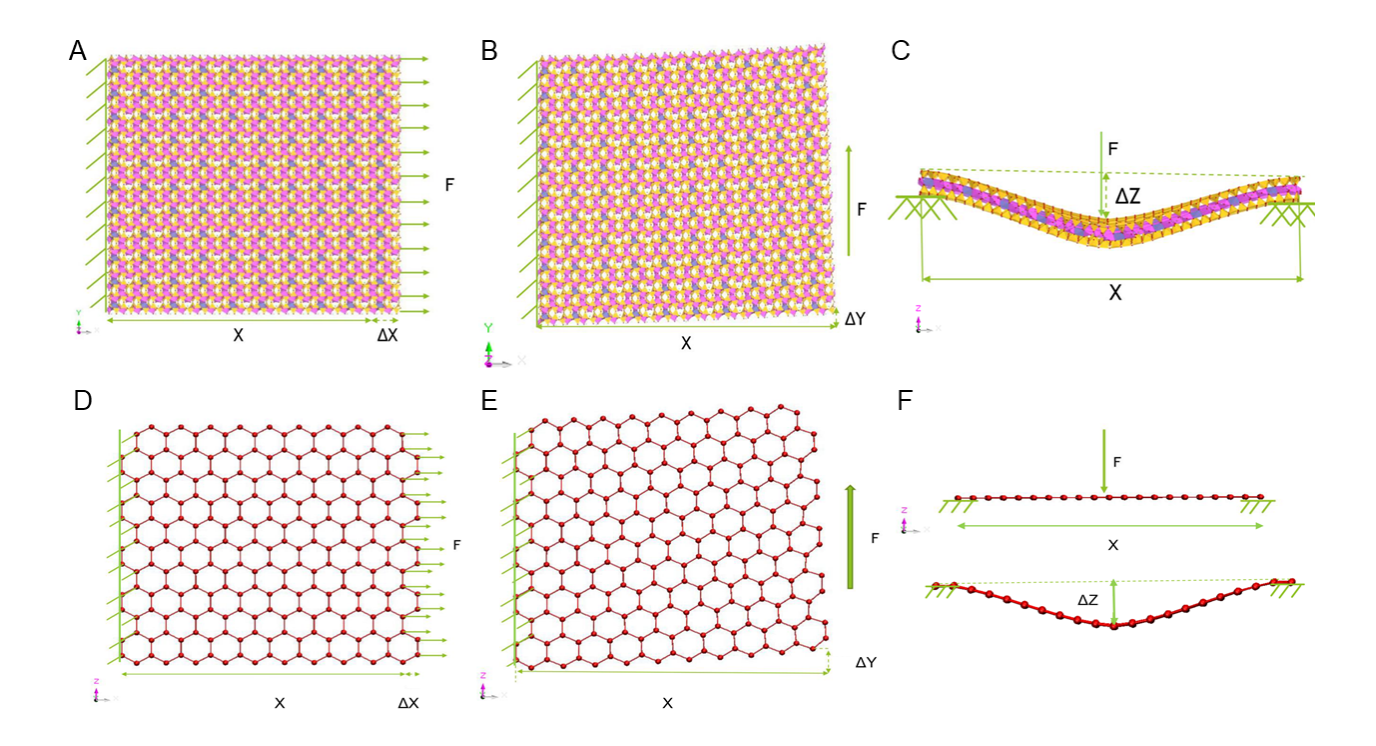


Figure 2. Evaluations of mechanical properties of Na-MMT model for the atomistic system under (A) tensile, (B) in-plane shearing, and (C) three-point bending. For the coarse-grained model under (D) tensilI(E) in-plane shearing, and (F) three-point bending.

With the in-plane mechanical properties obtained from AA model, we are able to estimate the bond and angle parameters k_r and k_θ based on the following relationships proposed by Gillis:⁶¹ $k_r = \sqrt{3} \, 2cES/2(4S-E)$ and $k_\theta = \sqrt{3} r_0^2 \, cES/12(3E-4S)$, where E is the tensile modulus, S is the in-plane shear modulus, and c is defined as twice the d-spacing with an initial value of 10 Å. The dihedral parameter k_ϕ is determined by matching the force-deflection $(F-\Delta Z)$ curves and thus bending rigidity of AA clay sheet. These three parameters are further refined and calibrated for the CG clay model by carrying out SMD simulations for the mechanical properties (**Figure 2D, E, F**). As a result, $k_r = 1560.43 \, \text{kcal/mol} \cdot \text{Å}^2$, $k_\theta = 2556.11 \, \text{kcal/mol} \cdot \text{rad}^2$ and $k_\phi = 591.05 \, \text{kcal/mol} \cdot \text{rad}^2$ are obtained for the CG model.

The non-bonded LJ parameters (ε and σ) for the CG model can be determined by preserving the interlayer adhesion energy and d-spacing in the AA clay tactoid. Here, a 10-layered AA clay tactoid model is simulated to evaluate the adhesion energy. Since the value of adhesion energy varies with the clay layer size, we normalize adhesion energy by the surface area. Through parametric analysis, the energetic parameter ε (i.e., the well depth of LJ potential) is estimated to be 9.75 kcal/mol to reproduce the AA normalized adhesion energy between the layers. The length scale parameter σ governs the equilibrium d-spacing of clay layers, which is determined to be 10.7 Å to match the AA d-spacing. **Table 1** summarizes all the functional forms and parameters of the CG force field.

Table 1. Functional forms and parameters of the CG force field.

Interaction	Functional form	Parameters	
Bond	$E_{\rm b} = k_r (r - r_0)^2$	$k_r = 1560.43 \text{ kcal/mol} \cdot \text{Å}^2$ $r_0 = 6.102 \text{ Å}$	
Angle	$E_{\rm a} = k_{\theta}(\theta - \theta_0)^2$	$k_{\theta} = 2556.11 \text{ kcal/mol} \cdot \text{rad}^2$ $\theta_0 = 120^{\circ}$	
Dihedral	$E_{\rm d} = k_{\varphi}[1 + \cos(n\varphi - \delta)]$	$k_{\varphi} = 591.05 \mathrm{kcal/mol \cdot rad^2}$ $\delta = 180^{\circ}$ n = 2	
Non-bonded	$E_{\rm nb} = 4\varepsilon \left[\left(\frac{\sigma}{r} \right)^{12} - \left(\frac{\sigma}{r} \right)^{6} \right], r < r_{cut}$	$arepsilon=9.75$ kcal/mol $\sigma=10.7 ext{Å}$ $r_{ ext{cut}}=17 ext{Å}$	

2.3. MD simulation details

Montmorillonite crystals belong to a 2:1 type layered aluminosilicate mineral, monoclinic system. The atomistic model of Na-MMT is built based on Swy-2 montmorillonite clay mineral obtained from a clay mineral repository at the University of Missouri, Columbia. The simplified structural formula of this atomistic model is NaSi₁₆(Al₆FeMg)O₂₀(OH)₄ and its unit cell

dimensions are $5.28 \text{ Å} \times 9.14 \text{ Å} \times 6.56 \text{ Å}$. Isomorphic substitution of Al³⁺ ions by Fe²⁺/Mg²⁺ ions generates a charge of -0.5e in each unit cell, neutralized by interlayer cations.^{33,62,63} The Materials Studio software is used to build the Na-MMT clay tactoid. All MD and SMD simulations are carried out utilizing Nanoscale Molecular Dynamics (NAMD)⁶⁴ and the Large-scale Atomic/Molecular Massively Parallel Simulator (LAMMPS)⁶⁵ software packages.

AA modeling. A total of three different atomistic models of Na-MMT have been utilized for the completion of this study. The first atomistic model is a 20×11 single clay sheet with the length and thickness of 100 Å and 6.56 Å respectively. This clay sheet of 8800 atoms is utilized for the determination of tensile modulus, in-plane shear modulus, and bending behavior. The second atomistic model is a 10-layer 6×3 atomistic Na-MMT clay tactoid, taken from an earlier study.¹⁷ The clay tactoid contains 7281 atoms with the dimensions of 31.68 $\text{Å} \times 27.44 \, \text{Å} \times 96.56 \, \text{Å}$. The tactoid model is utilized for calculating the non-bonded Lennard-Jones parameters (ε, σ) and a compressive modulus. Both first and second models are minimized and equilibrated at the temperature of 300 K and 101.325 kPa pressure under an isothermal-isobaric (NPT) ensemble for 2 ns. The time step is 0.5 fs and the Particle Mesh Ewald (PME) electrostatic interactions are implemented. In all the mechanical testing on these two models, a spring stiffness value of 9 kcal/mol/Å² and pulling velocity of 2 Å/ps are used for the SMD setting. These parameters of constant-velocity SMD are determined by the curve fitting method i.e., matching with the forcedisplacement curve of the constant-force method from the previous study.¹⁷ To calculate the interlayer shearing response, the third atomistic model that is a bi-layer system is considered. In this model, each layer is comprised of 2732 atoms with the dimensions of 41.09 $\text{Å} \times 36.24 \text{ Å}$ × 6.6 Å. The model is minimized and equilibrated under a canonical (NVT) ensemble for 1000000 steps at a temperature of 300 K. The time step of integration is 1 fs and the CLAYFF force field⁶⁶

is employed for atomistic modeling of clay. Both short-range and long-range interactions are estimated within a 17 Å cutoff. The electrostatic interactions are evaluated using the Ewald summation method⁶⁷ with a precision of 10^{-5} . Spring with the stiffness of $k_{\rm SMD} = 150 \, \rm kcal/mol/Å^2$ is attached to the center of mass of the top layer and pulled at a constant velocity of $10^{-5} \, \rm Å/fs$ using the SMD approach.

CG modeling. The initially built coarse-grained (CG) clay model is 100 Å in square sheet size with 229 beads. The purpose of this CG model is to determine the force field parameters through trial and error. Once the parameters have been determined, a larger CG clay sheet of 1,000 Å length has been built. This larger clay sheet comprising 19,700 beads is utilized to check the tensile modulus, in-plane shear modulus, and bending behavior of the CG model. A 10-layered CG tactoid model containing 197,000 beads is employed to determine non-bonded parameters and to inspect compressive modulus. The above-mentioned models are minimized using a conjugated gradient algorithm⁶⁸ and equilibrated at a temperature of 300 K and 1 atm pressure under the NPT ensemble for 6 ns. The time step for the integration is 3 fs for the CG-MD simulations. It is important to note that in all simulations, the non-bonded interactions between beads in the same sheets are ignored. To analyze the interlayer shearing properties of clay, a bi-layer CG system carrying 39,400 beads in total has been considered. The model is minimized and equilibrated at a temperature of 300 K under an NVT ensemble for 4 ns. To find appropriate values for pulling velocity and spring constant, we examined different values for SMD calculation. Due to the large dimension and high mass of each layer, the best spring constant and velocity to overcome the interlayer adhesion energy is 10,000 kcal/mol/ $Å^2$ and 10^{-5} Å/fs, respectively.

3. RESULTS AND DISCUSSION

Tensile Response. The correct prediction of bond-stretching and angle-bending parameters for the clay CG model can be reflected by the similar tensile response of AA and CG models. To check their tensile responses, both AA and CG equilibrated clay sheets are pulled along the positive x-direction while their left sides along the x-axis are kept fixed. The strain response is calculated as the ratio of extension (Δx) due to pulling along the x-axis and length of clay sheet along the xaxis (L_x) . The stress response is computed as the ratio of applied force (F) due to constant velocity and the cross-sectional area (A_{vz}) where the d-spacing is assumed as the thickness. As shown in Figure 3A, the tensile stress is increased approximately up to 6 GPa and the linear strain regime is observed until about 0.9% of tensile strain for both AA and CG models. The elastic modulus of tension for the AA clay sheet is determined as 695.8 GPa and the corresponding value for the CG model is found to be 703.9 GPa. This result shows that our CG model is working well and is in good agreement with AA model results. In another simulation study, Manevitch and Rutledge⁶⁹ calculated in-plane elastic modulus ranging from 400 GPa to 420 GPa for a single lamella of MMT based on the consistent valence force field (CVFF). The difference between the employed force fields may lead such inconsistence of modulus values between their study and our results. However, it should be noted that the tensile modulus of our CG model could be further tuned by varying the force constants in the bond and angle interactions as described in the above section.

In-plane-shear Response. The in-plane shear responses need to be similar between AA and CG models if the bond and angle parameters are correctly defined for CG clay. To compare the in-plane shear response of AA and CG clay models, the left side of both clay sheets along the x-axis is kept fixed while the right side is pulled along the positive y-axis. The strain response is computed as the extension (Δy) due to pulling along y-axis over the length of clay sheet along the

x-axis (L_x) . The stress response is recorded as the proportion of applied force (F) and the cross-sectional area (A_{yz}) on which it is applied. For both models, the maximum 4% in-plane shearing strain at an approximate corresponding stress of 5.8 GPa is considered for modulus calculations. As shown in **Figure 3B**, the in-plane shear moduli values for the AA model (137.23 GPa) and CG model (134.88 GPa) clearly depict the agreement between the models.

Bending Response. The similarity of bending behavior between the AA and CG model validates the prediction of the force field dihedral term of the CG model. To evaluate the bending response, a three-point bending test has been performed on both AA and CG clay sheets. This test is carried out by keeping two sides (along the x-axis) of clay sheets fixed while applying a vertical force at the midpoint of the clay sheet. The force is applied by employing constant velocity SMD $(k = 9 \text{ kcal/mol/Å}^2, v = 2 \text{ Å/ps})$. The bending response can be compared by following the applied force (F)-vertical deflection (Δz) path for both models. Both AA and CG models are gradually subjected to a force of about 245 nN resulting in an approximate vertical deflection of 13 Å (**Figure 3C**). The bending rigidity for the AA model and CG model is calculated as 2.8×10^{-17} N·m and 2.7×10^{-17} N·m, respectively. These values for bending property assures the agreement between the AA and CG models, which is also consistent with the work by Manevitch and Rutledge on the MD simulation of single MMT lamella.⁶⁹

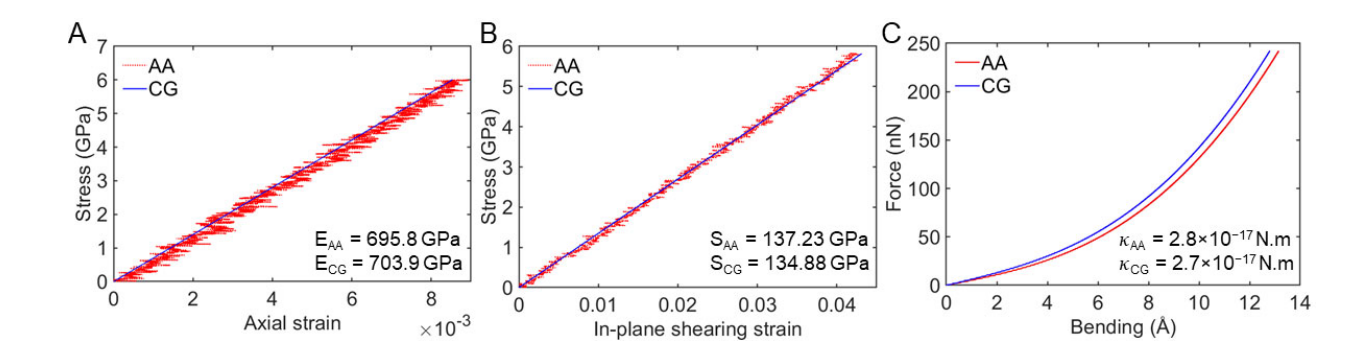


Figure 3. Comparison of the atomistic and coarse-grained clay model in terms of (A) tension, (B) in-plane shearing, and (C) three-point bending.

Interlayer Adhesion. The calculations of two LJ non-bonded parameters (ε and σ) for the CG model are done by preserving the adhesion energy of clay sheets and d-spacing of AA clay tactoid under coarse-graining. To evaluate the adhesion energy of the AA system, a 10-layered clay tactoid model is employed here. As shown in Figure 4, ¹⁷ for a 10-layer 6 × 3 AA Na-MMT model, the total absolute value of non-bonded energy for the bottommost layer (layer B) is determined as 1315 kcal/mol, after minimization and equilibration. It should be noted that this non-bonded energy consists of both clay-cation and clay-clay interaction energies. In this model, the total interacting area for this layer after bringing the clay system to the equilibrium is 984.23 Å². To make a comparison across different sizes, the adhesion energy normalized by the surface area is found to be 0.92 J/m² for the AA model. The target value of the parameter (ε) (i.e., the LJ well depth) of the CG model can thus be tuned to reproduce the AA normalized adhesion energy between the clay layers. The average d-spacing of the 10-layer AA clay is observed to be 10.8 Å, consistent with previous computational and experimental studies.^{17,70}

The relation between minimum potential distance (R_{\min}) and zero potential distance (σ) can be approximated as $R_{\min} = 2^{\frac{1}{6}} \sigma$, which can be further tuned to match the target d-spacing in the CG model.

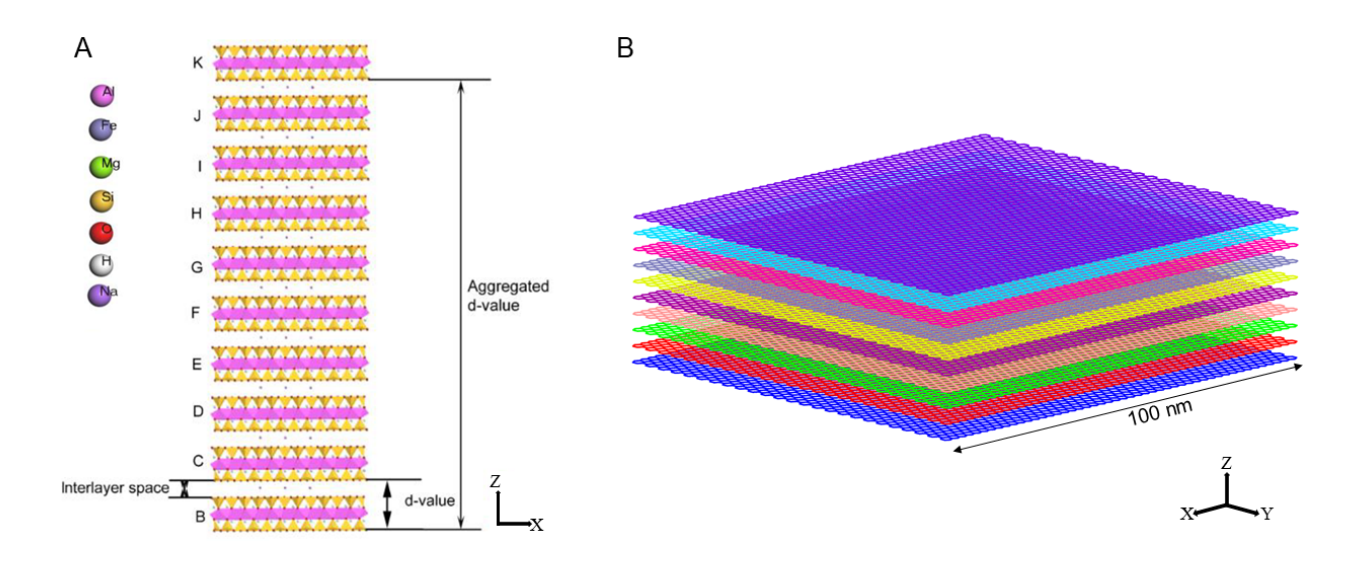


Figure 4. (A) Atomistic model of 10-layers Na-MMT from layer B to layer K, the color setting of constituent atoms presented in the left. (B) 10-layers CG model of Na-MMT tactoid.

Consistent with AA system, a 10-layered CG tactoid model with the length of 1000 Å is simulated to determine the non-bonded force field parameters (σ or R_{\min} and ε) for the CG model (**Figure 4B**). Since the CG model does not contain explicit interlayer cations, the effective CG clay-clay interaction energies should also include the clay-cation interaction energies. The equilibration of CG tactoid is performed for a range of values of σ and ε , where the normalized adhesion energy and d-spacing values are evaluated. **Figure 5A** shows that as σ increases, the d-spacing of the CG model tends to increase in a linear way. Similarly, the normalized adhesion energy increases as ε becomes larger in a near-linear fashion for all tested values of σ (**Figure 5B**). The final values of ε and σ are estimated to be 9.75 kcal/mol and 10.7 Å for the CG model,

respectively, to achieve the AA adhesion energy of 0.92 J/m² and d-spacing of 10.8 Å, respectively.¹⁷

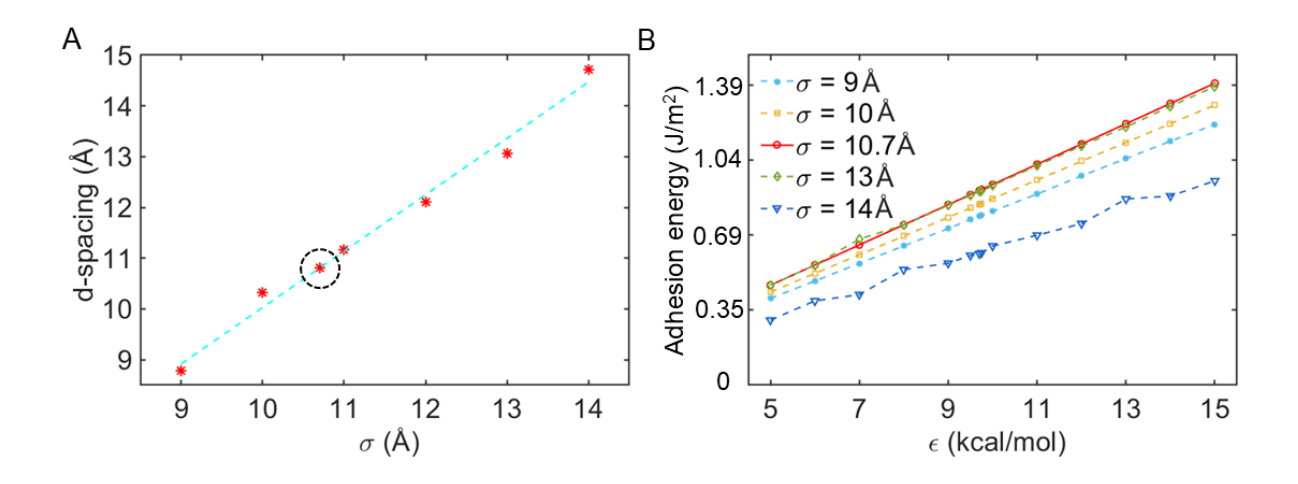


Figure 5. (A) Evaluation of d-spacing as a function of the nonbonded LJ potential length-scale parameter σ for the CG model. The target d-spacing of AA system is highlighted by the circle. (B) Evaluation of adhesion energy normalized by the surface area as a function of LJ potential energy parameter ε .

Interlayer Shear Analysis. We next carry out the interlayer shear simulations of AA and CG bilayer clay models using the constant-velocity SMD. During the shear deformation, the bottom layer is kept fixed while the top layer is pulled concerning a monotonous velocity in the x direction. Figure 6A, B show the snapshots of interlayer shear simulation for both AA and CG systems, respectively. The shear strain (γ_s) is determined as the ratio of incrementing distance (ΔX) regarding the equilibrium position in the pulling direction to the equilibrium d-spacing (10.8 Å). The shear stress (τ) can be defined as the x-component of pulling force (F) over the interacting surface area (A_{xy}) of clay sheet. Figure 6 shows the results of the shear stress versus strain for both AA and CG models. The shear modulus is determined by fitting the stress-strain data in the linear regime within 3% strain and the slopes of the curves, that plotted via dashed lines, indicate

the interlayer shear modulus of the bilayer systems. Using the obtained nonbonded LJ parameters that match the AA d-spacing and adhesion energy, the interlayer shear modulus of the CG model is found to be about 4 GPa, which is smaller than the AA shear modulus of 11.2 GPa. In order to mitigate this inconsistency, we further adjust the energetic parameter ε to preserve the AA interlayer shear modulus, leading to a second value of $\varepsilon = 60$ kcal/mol. The blue curve in **Figure 6C** shows the shear stress versus strain of the CG model with the value of ε by matching the adhesion energy with the AA model; the green curve is the interlayer shear response of the CG model with the ε to match the AA shear modulus. Therefore, we report two ε values for our CG model: one for preserving the interlayer adhesion and the other one for preserving the interlayer shear modulus.

Interestingly, **Figure 6C** shows strong evidence of "stick-slip" behaviors during the interlayer shear deformation for the clay systems. The AA clay model contains the interlayer cations arranged symmetrically along the xy plane between the clay layers. When the shear force is imposed on the top clay layer along the x-axis, it starts to move in the same direction while the first row of sodium ions tends to lock the movement of the clay layer. As a result, an initial steep upward stress-strain curve is observed, corresponding to the linear elastic regime. The continuous pulling ultimately causes the clay layer to overcome the restraining effect of cations and the clay layer moved freely, which is characterized by the downfall of the stress-strain curve. As the clay layer further moves towards the pulling direction, the second row of cations tried to lock its motion again, and eventually, the clay layer overcame this locking effect. The second uphill and downhill portions of the stress-strain curve clearly reflect such "stick-slip" phenomena. Remarkably, such shear characteristics are well captured by the much "simplified" CG model even without explicitly incorporating cations. In the CG model, the interlayer interactions between the beads in the bottom

and top layers effectively capture the potential energy landscape due to the hexagonal lattice geometry of CG clay sheets. To overcome the potential energy barrier, the pulling or shear force increases gradually, leading to an upward trend of the stress-strain curve in the CG model; once the pulling force overcomes this energy barrier, the stress-strain curve drops suddenly. This result indicates the importance of the lattice geometry and interlayer interaction in the interlayer shear response of CG clays, especially beyond the linear elastic regime.

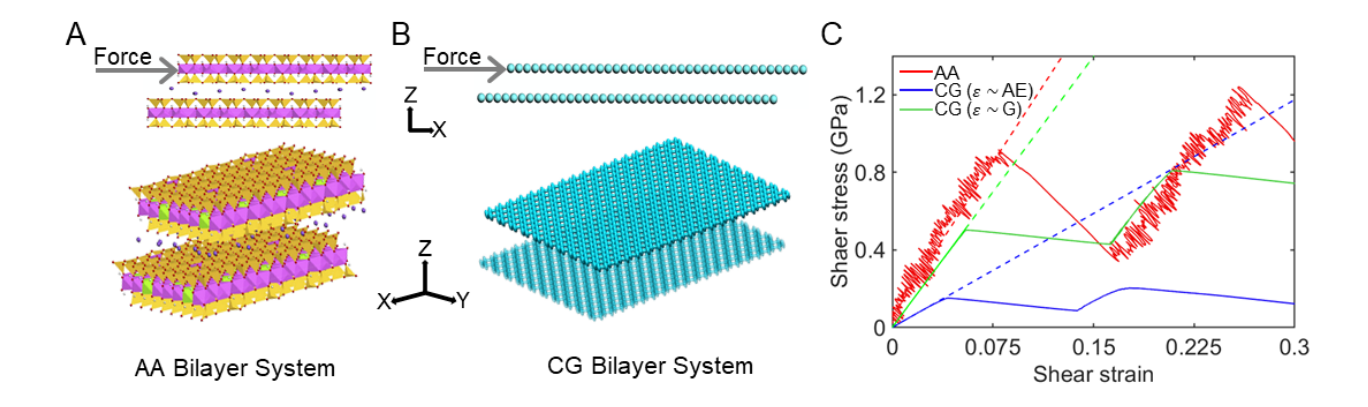


Figure 6. Comparison of the AA and CG clay tactoid in terms of interlayer shearing. A sequence of snapshots illustrating the shear deformation process for (A) AA bilayer simulation and (B) CG bilayer system. (C) Shear stress vs shear strain curves for AA and CG with different ε values. The dashed lines indicate the slope of the linear regime for the determination of interlayer shear modulus.

Compressive Response. As the clay tactoid is often subject to high pressure condition, here, we evaluate the compressive response of the CG model in comparison with AA one using the 10-layered clay tactoid model systems. In both cases, the compression is performed by keeping the bottom clay layer (layer B) fixed while applying force on the top clay layer (labeled as layer K) in the vertically downward direction. A range of forces (0 - 2500 pN) is applied on AA tactoid utilizing constant-velocity SMD. **Figure 7** shows that four different compressive stress-strain

regions are observed in the AA system, characterized by the apparent moduli of 125 GPa, 237.5 GPa, 411 GPa, and 643 GPa, respectively. Different from the AA model, the CG model displays only a linear regime of compressive stress-strain with an elastic modulus of 112.95 GPa. It is observed that the CG model mostly reproduces only the first regime (0 - 1.76 GPa of stress) of AA response. The compression mechanism of AA clay tactoid has been discussed in the previous study. 17 During the compression of the AA model, the first domain of stress-strain response (0 -2.22 GPa) represents the initial compression of interlayer space while the later domains (2.22-5.92, 5.92-14.8, and 14.8-29.6 GPa) represent full compression of effective interlayer space by pushing the interlayer cations into ditrigonal cavities of clay sheets. Different from the AA model, the CG clay model retains the combined clay-cation and clay-clay atomistic interactions between the CG clay layers by employing suitable non-bonded parameters (ε, σ) rather than containing any explicit interlayer cations. As a result, the current clay CG model only exhibits a single compressive modulus for the first elastic regime in the AA model but not the higher moduli response beyond the first elastic regime. However, in real-life conditions, the clays rarely undergo such very high-stress conditions, and thus, this CG clay model can still be utilized to simulate the compressive behavior of clays under low stress and deformation condition to a good approximation. Table 2 summarizes all mechanical properties obtained from our AA and CG simulations as well as the reported values from literatures if available.

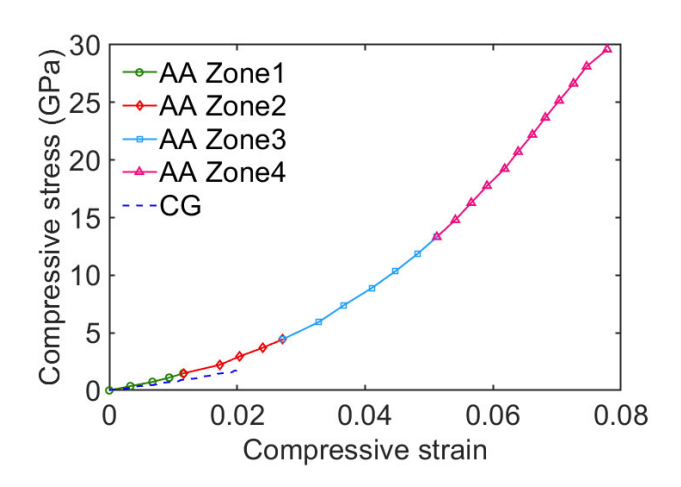


Figure 7. Comparison of the AA and CG clay tactoid models for compression. Different observed zones for AA system corresponds to various ranges of applied stress, including 0 - 2.22, 2.22 - 5.92, 5.92 - 14.8, and 14.8 - 29.6 GPa.

Table 2. Mechanical properties of AA and CG models compared with previous experimental and computational results.

Properties	AA	CG	Reported values
Tensile modulus (GPa)	695.8	703.9	$400 - 420^{69}$ (a)
In-plane shear modulus (GPa)	137.2	134.9	N/A
Bending rigidity (N·m)	2.8×10^{-17}	2.7×10^{-17}	1.25×10^{-17} 69 (a)
Compressive modulus (GPa)	125	113	N/A
Interlayer shear modulus (GPa)	11.2	10.9	15.6 ^{71 (b)}
d-spacing (Å)	10.8	10.8	9.7 ^{70 (b)}
Interlayer adhesion (J/m ²)	0.92	0.92	N/A

N/A = not available; (a) = Computational data, (b) = Experimental data

Computational performance. One of the key advantages of CG modeling is the speed-up in computation because of the reduction of the number of beads that leads to reducing the total number of degrees of freedom and interactions. Another way to speed up can be reached by

utilizing a larger timestep in CG-MD simulations due to the relatively "smooth" energy landscape associated with the CG force field. In order to comparison CPU time between AA and CG systems, a multilayer clay system with different sizes in dimensions ranging from 10 Å to 1000 Å is simulated. To make a comparison, the first 50 ps of the simulation is considered using 10 CPUs. **Figure 8** shows that there is a linear trend between clay sheet dimension and CPU time in the logarithmic scale; as we increase the clay sheet size, the CPU time for CG models varies by a gentle slope, whereas the AA systems have a steeper slope of the curve. As one can see, using the CG models for MD calculations is significantly faster in computation compared to AA models. For instance, for the clay sheet with a dimension of 100 Å, the CPU time of AA simulation is about 6500 times as much as the CG simulation. The equations of fitted lines to the data are shown in **Figure 8** caption as well, where one can predict the CPU time for larger clay sheet sizes. This comparison makes it obvious that the current CG model will be greatly advantageous for simulating more realistic clay-based systems (such as polymer-clay nanocomposites) with larger length and time scales.

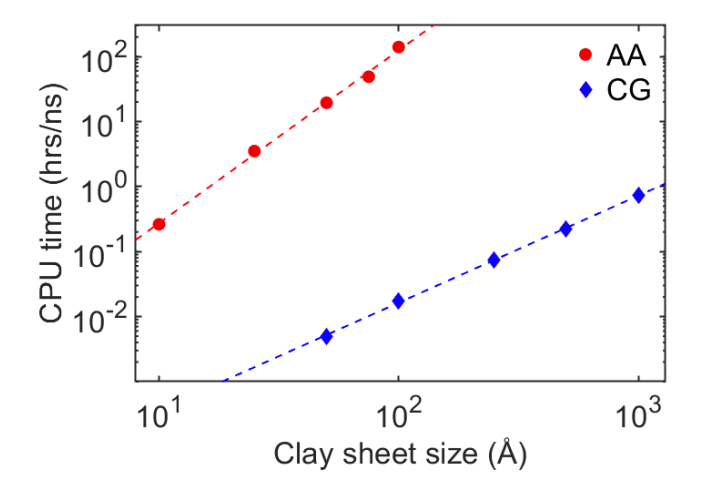


Figure 8. Comparison of the AA and CG clay model with 50 ps simulation time utilizing 10 CPUs and 10 processors. The dashed lines represent the fitting lines to the data via the equations: y =

 $e^{-7.41}x^{2.66}$ and $y = e^{-11.7}x^{1.65}$ for AA and CG systems, respectively. The coefficient of determination (R^2) of the fitting for AA and CG models are calculated to be 0.83 and 0.97, respectively.

Compared to the previously developed CG clay models, our CG model has several advantages. Different from previous CG models that often involve diverse types of beads and interactions, 49, ^{50,53} our developed CG model is largely simplified by considering only one bead type, and thus it can achieve significant improvement in computation, making it more suitable for modeling largesized clay sheets relevant to experimental scales. At the same time, the current CG model is capable of preserving the structural, mechanical and interlayer characteristics of the layered clay, which has not been carefully considered in previous relevant studies. 42,49,72 More importantly, the established modeling framework in this study can be readily extended and applied for modeling other relevant clay minerals systems such as kaolinite and silica sheets with parametrization of intralayer and interlayer interactions. Since our CG model can preserve the out-of-plane bending of the clay sheets, it is possible to study the curvature effect on the mechanical behavior of the clay, similar to the study by Ferrante et al. 73 on the distortion of halloysite clay nanotubes (HNTs) based on atomistic modeling. Previous studies have also employed the CG modeling to investigate the hydration behavior of clay minerals. 74–78 Our CG model of Na-MMT clay can also be extended for this purpose by either reparameterization of the interlayer interaction to effectively capture the clay-water phenomena in an implicit manner or adding "explicit" AA or CG water models (e.g., MARTINI water model⁷⁹) to the clay system. A similar kind of approach was undertaken to study the behavior of graphene/graphene oxide in an aqueous solution. 80 Since our modeling framework is based on AA system using the ClayFF where some internal multipole moments in clay minerals

are misinterpreted,^{39,66,81} the predictive accuracy of CG model might need to be improved for consideration of the interfacial interactions with solvents and organic molecules.

4. CONCLUSION

In this study, we employ the strain energy conservation approach to develop an atomistically informed CG model of Na-MMT clay mineral that effectively mimics the mechanical and structural characteristics of the atomistic model. Specifically, the bonded interactions (including bond, angle, and dihedral terms) of the CG force field are derived by preserving the in-plain elastic constants, while the nonbonded interaction is derived by preserving the d-spacing and interlayer adhesion between clay particles. The developed CG model can capture both in-plane and interlayer mechanical properties of the AA model, including tension, in-plane-shear, bending, interlayer shear and adhesion, and compression in the elastic regime, which are also consistent with the previous studies. Remarkably, the CG model has drastically reduced the simulation time and thereby make it possible to simulate the properties of large-sized environmentally found montmorillonite clay minerals. Our proposed CG modeling framework highlights the efficacy of CG models with tremendous speed-up in computation compared to the AA systems, paving the way for bottom-up and multiscale prediction of mechanical behaviors of nanoclay and related minerals.

ACKNOLWEDGEMENT

This work was supported by the National Science Foundation (NSF) under NSF OIA ND-ACES Award No. 1946202. S.G. and W.X. acknowledged the support from the North Dakota Established Program to Stimulate Competitive Research (ND EPSCoR) through the New Faculty Award, the Department of Civil, Construction and Environmental Engineering, and the College of Engineering at North Dakota State University (NDSU). S.G. acknowledged the Cyberinfrastructure Assistantship Award from ND EPSCoR. This work used supercomputing resources of the CCAST at NDSU, which were made possible in part by NSF MRI Award No. 2019077.

References

- (1) Grim, R. E. Clay Mineralogy: 2nd Edn McGraw-Hill. New York 1968.
- (2) Buzzi, O.; Fityus, S.; Sloan, S. W. Use of Expanding Polyurethane Resin to Remediate Expansive Soil Foundations. *Can. Geotech. J.* **2010**, *47* (6), 623–634.
- (3) Bowders, J. J.; Tan, J. P.; Daniel, D. E. Expanded Clay and Shale Aggregates for Leachate Collection Systems. *J. Geotech. geoenvironmental Eng.* **1997**, *123* (11), 1030–1034.
- (4) Daniel, D. E. Effects of Partial Wetting on the Performance of the Bentonite Component of a Geosynthetic Clay Liner. In *Geosynthetics'* 93; IFAI, 1993; pp 1482–1496.
- (5) Wang, S.; Hu, Y.; Wang, Z.; Yong, T.; Chen, Z.; Fan, W. Synthesis and Characterization of Polycarbonate/ABS/Montmorillonite Nanocomposites. *Polym. Degrad. Stab.* **2003**, *80* (1), 157–161.
- (6) Zhang, J.; Wilkie, C. A. Preparation and Flammability Properties of Polyethylene–Clay Nanocomposites. *Polym. Degrad. Stab.* **2003**, *80* (1), 163–169.
- (7) Liu, T.; Lim, K. P.; Tjiu, W. C.; Pramoda, K. P.; Chen, Z.-K. Preparation and Characterization of Nylon 11/Organoclay Nanocomposites. *Polymer (Guildf)*. 2003, 44 (12), 3529–3535.
- (8) Okada, A.; Kawasumi, M.; Usuki, A.; Kojima, Y.; Kurauchi, T.; Kamigaito, O. Nylon 6–Clay Hybrid. *MRS Online Proc. Libr.* **1989**, *171*, 45–50.
- (9) Park, H.-M.; Lee, W.-K.; Park, C.-Y.; Cho, W.-J.; Ha, C.-S. Environmentally Friendly Polymer Hybrids Part I Mechanical, Thermal, and Barrier Properties of Thermoplastic Starch/Clay Nanocomposites. *J. Mater. Sci.* **2003**, *38* (5), 909–915.

- (10) Massat, L.; Cuisinier, O.; Bihannic, I.; Claret, F.; Pelletier, M.; Masrouri, F.; Gaboreau, S. Swelling Pressure Development and Inter-Aggregate Porosity Evolution upon Hydration of a Compacted Swelling Clay. *Appl. Clay Sci.* 2016, 124, 197–210.
- (11) Bihannic, I.; Tchoubar, D.; Lyonnard, S.; Besson, G.; Thomas, F. X-Ray Scattering Investigation of Swelling Clay Fabric: 1. The Dry State. *J. Colloid Interface Sci.* **2001**, 240 (1), 211–218.
- (12) Cases, J. M.; Bérend, I.; Besson, G.; Francois, M.; Uriot, J. P.; Thomas, F.; Poirier, J. E. Mechanism of Adsorption and Desorption of Water Vapor by Homoionic Montmorillonite. 1. The Sodium-Exchanged Form. *Langmuir* 1992, 8 (11), 2730–2739.
- (13) Keller, L. M.; Schuetz, P.; Erni, R.; Rossell, M. D.; Lucas, F.; Gasser, P.; Holzer, L. Characterization of Multi-Scale Microstructural Features in Opalinus Clay. *Microporous mesoporous Mater.* **2013**, *170*, 83–94.
- (14) Likos, W. J.; Wayllace, A. Porosity Evolution of Free and Confined Bentonites during Interlayer Hydration. *Clavs Clay Miner.* **2010**, *58* (3), 399–414.
- (15) Grim, R. E. Modern Concepts of Clay Materials. J. Geol. **1942**, 50 (3), 225–275.
- (16) Hendricks, S. B.; Jefferson, M. E. Structures of Kaolin and Talc-Pyrophyllite Hydrates and Their Bearing on Water Sorption of the Clays. *Am. Mineral. J. Earth Planet. Mater.*1938, 23 (12), 863–875.
- (17) Faisal, H. M. N.; Katti, K. S.; Katti, D. R. Molecular Mechanics of the Swelling Clay Tactoid under Compression, Tension and Shear. *Appl. Clay Sci.* **2020**, *200*, 1–12.
- (18) Jonas, E. C.; Oliver, R. M. Size and Shape of Montmorillonite Crystallites. *Clays Clay*

- *Miner.* **1967**, *15* (1), 27–33.
- (19) Perdrial, J. N.; Warr, L. N. Hydration Behavior of MX80 Bentonite in a Confined-Volume System: Implications for Backfill Design. *Clays Clay Miner.* **2011**, *59* (6), 640–653.
- (20) Michot, L. J.; Bihannic, I.; Porsch, K.; Maddi, S.; Baravian, C.; Mougel, J.; Levitz, P.
 Phase Diagrams of Wyoming Na-Montmorillonite Clay. Influence of Particle Anisotropy.
 Langmuir 2004, 20 (25), 10829–10837.
- (21) Cadene, A.; Durand-Vidal, S.; Turq, P.; Brendle, J. Study of Individual Na-Montmorillonite Particles Size, Morphology, and Apparent Charge. *J. Colloid Interface Sci.* **2005**, *285* (2), 719–730.
- (22) Segad, M.; Jönsson, B.; Cabane, B. Tactoid Formation in Montmorillonite. *J. Phys. Chem.*C 2012, 116 (48), 25425–25433.
- (23) Faisal, H. M. N.; Katti, K. S.; Katti, D. R. Modeling the Behavior of Organic Kerogen in the Proximity of Calcite Mineral by Molecular Dynamics Simulations. *Energy & Fuels* **2020**, *34* (3), 2849–2860.
- (24) Faisal, H. M. N.; Katti, K. S.; Katti, D. R. An Insight into Quartz Mineral Interactions with Kerogen in Green River Oil Shale. *Int. J. Coal Geol.* **2021**, *238*, 1–10.
- (25) Suter, J. L.; Anderson, R. L.; Greenwell, H. C.; Coveney, P. V. Recent Advances in Large-Scale Atomistic and Coarse-Grained Molecular Dynamics Simulation of Clay Minerals. J. Mater. Chem. 2009, 19 (17), 2482–2493.
- (26) Bitinis, N.; Hernández, M.; Verdejo, R.; Kenny, J. M.; Lopez-Manchado, M. A. Recent Advances in Clay/Polymer Nanocomposites. *Adv. Mater.* **2011**, *23* (44), 5229–5236.

- (27) Saadatfar, M.; Soleimani, A. Effective Parameters on Elastic Modulus of Polymer/Clay Nanocomposites. In *Advanced Materials Research*; Trans Tech Publ, 2012; Vol. 403, pp 4416–4420.
- (28) Anderson, R. L.; Ratcliffe, I.; Greenwell, H. C.; Williams, P. A.; Cliffe, S.; Coveney, P. V. Clay Swelling—a Challenge in the Oilfield. *Earth-Science Rev.* **2010**, *98* (3–4), 201–216.
- (29) Katti, D. R.; Katti, K. S.; Thapa, K. B.; Faisal, H. M.; Consortium, M. P. Development of Models for the Prediction of Shear Strength of Swelling Clays; Mountain Plains Consortium, 2019.
- (30) Katti, D. R.; Ghosh, P.; Schmidt, S.; Katti, K. S. Mechanical Properties of the Sodium Montmorillonite Interlayer Intercalated with Amino Acids. *Biomacromolecules* **2005**, *6* (6), 3276–3282.
- (31) Katti, D. R.; Schmidt, S. R.; Ghosh, P.; Katti, K. S. Modeling the Response of Pyrophyllite Interlayer to Applied Stress Using Steered Molecular Dynamics. *Clays Clay Miner.* **2005**, *53* (2), 171–178.
- (32) Katti, D. R.; Schmidt, S. R.; Ghosh, P.; Katti, K. S. Molecular Modeling of the Mechanical Behavior and Interactions in Dry and Slightly Hydrated Sodium Montmorillonite Interlayer. *Can. Geotech. J.* 2007, 44 (4), 425–435.
- (33) Schmidt, S. R.; Katti, D. R.; Ghosh, P.; Katti, K. S. Evolution of Mechanical Response of Sodium Montmorillonite Interlayer with Increasing Hydration by Molecular Dynamics. *Langmuir* **2005**, *21* (17), 8069–8076.

- (34) Katti, D. R.; Patwary, Z. R.; Katti, K. S. Modelling Clay–Fluid Interactions in Montmorillonite Clays. *Environ. Geotech.* **2016**, *4* (5), 322–338.
- (35) Katti, D. R.; Thapa, K. B.; Katti, K. S. The Role of Fluid Polarity in the Swelling of Sodium-Montmorillonite Clay: A Molecular Dynamics and Fourier Transform Infrared Spectroscopy Study. *J. Rock Mech. Geotech. Eng.* **2018**, *10* (6), 1133–1144.
- (36) Heinz, H.; Koerner, H.; Anderson, K. L.; Vaia, R. A.; Farmer, B. L. Force Field for Mica-Type Silicates and Dynamics of Octadecylammonium Chains Grafted to Montmorillonite. *Chem. Mater.* **2005**, *17* (23), 5658–5669. https://doi.org/10.1021/cm0509328.
- (37) Dongol, R.; Wang, L.; Cormack, A. N.; Sundaram, S. K. Molecular Dynamics Simulation of Sodium Aluminosilicate Glass Structures and Glass Surface-Water Reactions Using the Reactive Force Field (ReaxFF). *Appl. Surf. Sci.* **2018**, *439*, 1103–1110.
- (38) Heinz, H. Clay Minerals for Nanocomposites and Biotechnology: Surface Modification,
 Dynamics and Responses to Stimuli. *Clay Miner.* **2012**, *47* (2), 205–230.
- (39) Mishra, R. K.; Mohamed, A. K.; Geissbühler, D.; Manzano, H.; Jamil, T.; Shahsavari, R.; Kalinichev, A. G.; Galmarini, S.; Tao, L.; Heinz, H. Cemff: A Force Field Database for Cementitious Materials Including Validations, Applications and Opportunities. *Cem. Concr. Res.* **2017**, *102*, 68–89.
- (40) Pustovgar, E.; Mishra, R. K.; Palacios, M.; de Lacaillerie, J.-B. d'Espinose; Matschei, T.; Andreev, A. S.; Heinz, H.; Verel, R.; Flatt, R. J. Influence of Aluminates on the Hydration Kinetics of Tricalcium Silicate. *Cem. Concr. Res.* **2017**, *100*, 245–262.
- (41) Heinz, H.; Lin, T.-J.; Kishore Mishra, R.; Emami, F. S. Thermodynamically Consistent

- Force Fields for the Assembly of Inorganic, Organic, and Biological Nanostructures: The INTERFACE Force Field. *Langmuir* **2013**, *29* (6), 1754–1765.
- (42) Thyveetil, M.-A.; Coveney, P. V; Suter, J. L.; Greenwell, H. C. Emergence of Undulations and Determination of Materials Properties in Large-Scale Molecular Dynamics Simulation of Layered Double Hydroxides. *Chem. Mater.* **2007**, *19* (23), 5510–5523.
- (43) Freeman, C. L.; Harding, J. H.; Cooke, D. J.; Elliott, J. A.; Lardge, J. S.; Duffy, D. M. New Forcefields for Modeling Biomineralization Processes. *J. Phys. Chem. C* **2007**, *111* (32), 11943–11951.
- (44) Voth, G. A. Coarse-Graining of Condensed Phase and Biomolecular Systems; CRC press, 2008.
- (45) Nielsen, S. O.; Lopez, C. F.; Srinivas, G.; Klein, M. L. Coarse Grain Models and the Computer Simulation of Soft Materials. *J. Phys. Condens. Matter* **2004**, *16* (15), R481–R512.
- (46) Müller-Plathe, F. Coarse-Graining in Polymer Simulation: From the Atomistic to the Mesoscopic Scale and Back. *ChemPhysChem* **2002**, *3* (9), 754–769.
- (47) Alesadi, A.; Xia, W. Understanding the Role of Cohesive Interaction in Mechanical Behavior of a Glassy Polymer. *Macromolecules* **2020**, *53* (7), 2754–2763.
- (48) Liao, Y.; Li, Z.; Ghazanfari, S.; Fatima; Croll, A. B.; Xia, W. Understanding the Role of Self-Adhesion in Crumpling Behaviors of Sheet Macromolecules. *Langmuir* 2021, 37 (28), 8627–8637.
- (49) Jardat, M.; Dufrêche, J.-F.; Marry, V.; Rotenberg, B.; Turq, P. Salt Exclusion in Charged

- Porous Media: A Coarse-Graining Strategy in the Case of Montmorillonite Clays. *Phys. Chem. Chem. Phys.* **2009**, *11* (12), 2023–2033.
- (50) Liu, C. An Ion Diffusion Model in Semi-Permeable Clay Materials. *Environ. Sci. Technol.*2007, 41 (15), 5403–5409.
- (51) Sheng, N.; Boyce, M. C.; Parks, D. M.; Rutledge, G. C.; Abes, J. I.; Cohen, R. E. Multiscale Micromechanical Modeling of Polymer/Clay Nanocomposites and the Effective Clay Particle. *Polymer (Guildf)*. **2004**, *45* (2), 487–506.
- (52) Suter, J. L.; Groen, D.; Coveney, P. V. Mechanism of Exfoliation and Prediction of Materials Properties of Clay–Polymer Nanocomposites from Multiscale Modeling. *Nano Lett.* 2015, 15 (12), 8108–8113.
- (53) Suter, J. L.; Groen, D.; Coveney, P. V. Chemically Specific Multiscale Modeling of Clay–Polymer Nanocomposites Reveals Intercalation Dynamics, Tactoid Self-Assembly and Emergent Materials Properties. *Adv. Mater.* **2015**, *27* (6), 966–984.
- (54) Ebrahimi, D.; Whittle, A. J.; Pellenq, R. J.-M. Mesoscale Properties of Clay Aggregates from Potential of Mean Force Representation of Interactions between Nanoplatelets. *J. Chem. Phys.* **2014**, *140* (15), 154309.
- (55) Ebrahimi, D.; Pellenq, R. J.-M.; Whittle, A. J. Mesoscale Simulation of Clay Aggregate Formation and Mechanical Properties. *Granul. Matter* **2016**, *18* (3), 1–8.
- (56) Schaettle, K.; Ruiz Pestana, L.; Head-Gordon, T.; Lammers, L. N. A Structural Coarse-Grained Model for Clays Using Simple Iterative Boltzmann Inversion. *J. Chem. Phys.* 2018, 148 (22), 222809.

- (57) Khan, P.; Goel, G. Martini Coarse-Grained Model for Clay–Polymer Nanocomposites. *J. Phys. Chem. B* **2019**, *123* (42), 9011–9023.
- (58) Ruiz, L.; Xia, W.; Meng, Z.; Keten, S. A Coarse-Grained Model for the Mechanical Behavior of Multi-Layer Graphene. *Carbon N. Y.* **2015**, *82*, 103–115.
- (59) Weiner, J. H. Statistical Mechanics of Elasticity; Courier Corporation, 2012.
- (60) Izrailev, S.; Stepaniants, S.; Isralewitz, B.; Kosztin, D.; Lu, H.; Molnar, F.; Wriggers, W.; Schulten, K. Computational Molecular Dynamics: Challenges, Methods. In *Ideas*; 1998; Vol. 4, p 39.
- (61) Gillis, P. P. Calculating the Elastic Constants of Graphite. *Carbon N. Y.* **1984**, *22* (4–5), 387–391.
- (62) Katti, D. R.; Shanmugasundaram, V. Influence of Swelling on the Microstructure of Expansive Clays. *Can. Geotech. J.* **2001**, *38* (1), 175–182.
- (63) Skipper, N. T.; Chang, F.-R. C.; Sposito, G. Monte Carlo Simulation of Interlayer
 Molecular Structure in Swelling Clay Minerals. 1. Methodology. *Clays Clay Miner.* 1995,
 43 (3), 285–293.
- (64) Phillips, J. C.; Braun, R.; Wang, W.; Gumbart, J.; Tajkhorshid, E.; Villa, E.; Chipot, C.; Skeel, R. D.; Kale, L.; Schulten, K. Scalable Molecular Dynamics with NAMD. *J. Comput. Chem.* **2005**, *26* (16), 1781–1802.
- (65) Plimpton, S. Fast Parallel Algorithms for Short-Range Molecular Dynamics. *J. Comput. Phys.* **1995**, *117* (1), 1–19.
- (66) Cygan, R. T.; Liang, J.-J.; Kalinichev, A. G. Molecular Models of Hydroxide,

- Oxyhydroxide, and Clay Phases and the Development of a General Force Field. *J. Phys. Chem. B* **2004**, *108* (4), 1255–1266.
- (67) Plimpton, S.; Pollock, R.; Stevens, M. Particle-Mesh Ewald and RRESPA for Parallel Molecular Dynamics Simulations. In *PPSC*; Citeseer, 1997; pp 1–13.
- (68) Payne, M. C.; Teter, M. P.; Allan, D. C.; Arias, T. A.; Joannopoulos, ad J. D. Iterative Minimization Techniques for Ab Initio Total-Energy Calculations: Molecular Dynamics and Conjugate Gradients. *Rev. Mod. Phys.* **1992**, *64* (4), 1045–1097.
- (69) Manevitch, O. L.; Rutledge, G. C. Elastic Properties of a Single Lamella of Montmorillonite by Molecular Dynamics Simulation. J. Phys. Chem. B 2004, 108 (4), 1428–1435.
- (70) Amarasinghe, P. M.; Katti, K. S.; Katti, D. R. Molecular Hydraulic Properties of Montmorillonite: A Polarized Fourier Transform Infrared Spectroscopic Study. *Appl. Spectrosc.* 2008, 62 (12), 1303–1313.
- (71) Mondol, N. H.; Jahren, J.; Bjørlykke, K.; Brevik, I. Elastic Properties of Clay Minerals. *Lead. Edge* **2008**, *27* (6), 758–770.
- (72) Suter, J. L.; Coveney, P. V; Greenwell, H. C.; Thyveetil, M.-A. Large-Scale Molecular Dynamics Study of Montmorillonite Clay: Emergence of Undulatory Fluctuations and Determination of Material Properties. *J. Phys. Chem. C* **2007**, *111* (23), 8248–8259.
- (73) Ferrante, F.; Armata, N.; Lazzara, G. Modeling of the Halloysite Spiral Nanotube. *J. Phys. Chem. C* **2015**, *119* (29), 16700–16707.
- (74) Riniker, S.; van Gunsteren, W. F. A Simple, Efficient Polarizable Coarse-Grained Water

- Model for Molecular Dynamics Simulations. J. Chem. Phys. 2011, 134 (8), 84110.
- (75) Sun, H.; Yang, W.; Chen, R.; Kang, X. A Coarse-Grained Water Model for Mesoscale Simulation of Clay-Water Interaction. *J. Mol. Liq.* **2020**, *318*, 1–8.
- (76) Wu, Z.; Cui, Q.; Yethiraj, A. A New Coarse-Grained Model for Water: The Importance of Electrostatic Interactions. *J. Phys. Chem. B* **2010**, *114* (32), 10524–10529.
- (77) Zavadlav, J.; Melo, M. N.; Marrink, S. J.; Praprotnik, M. Adaptive Resolution Simulation of Polarizable Supramolecular Coarse-Grained Water Models. *J. Chem. Phys.* 2015, *142* (24), 06B622 1.
- (78) Kang, X.; Sun, H.; Yang, W.; Chen, R. Wettability of Clay Aggregates—A Coarse-Grained Molecular Dynamic Study. *Appl. Surf. Sci.* **2020**, *532*, 147423.
- (79) Yesylevskyy, S. O.; Schäfer, L. V; Sengupta, D.; Marrink, S. J. Polarizable Water Model for the Coarse-Grained MARTINI Force Field. *PLoS Comput. Biol.* **2010**, *6* (6), 1–17.
- (80) Williams, C. D.; Lísal, M. Coarse Grained Models of Graphene and Graphene Oxide for Use in Aqueous Solution. *2D Mater.* **2020**, *7* (2), 1–16.
- (81) Kalinichev, A. G.; Kirkpatrick, R. J.; Cygan, R. T. Molecular Modeling of the Structure and Dynamics of the Interlayer and Surface Species of Mixed-Metal Layered Hydroxides: Chloride and Water in Hydrocalumite (Friedel's Salt). *Am. Mineral.* **2000**, *85* (7–8), 1046–1052.

Table of Content Figure

